Title
COMBINED CORROSION-EROSION OF STEELS IN OXIDIZING ENVIRONMENTS

Authors
Levy, A.V.
Slairovich, E.

Publication Date
1984-04-01

Lawrence Berkeley Laboratory
UNIVERSITY OF CALIFORNIA

Materials & Molecular Research Division

Submitted to Wear

COMBINED CORROSION-EROSION OF STEELS IN OXIDIZING ENVIRONMENTS

A.V. Levy and E. Slamovich

April 1984

Prepared for the U.S. Department of Energy under Contract DE-AC03-76SF00098

DISCLAIMER

LBL 15657

COMBINED CORROSION-EROSION OF STEELS IN OXIDIZING ENVIRONMENTS

Alan V. Levy and Elliott Slamovich

Materials and Molecular Research Division
Lawrence Berkeley Laboratory
University of California
Berkeley, California 94720

Research sponsored by the Department of Energy under DOE/FEAA 15 10 10 0, Advanced Research and Technical Development, Fossil Energy Materials Program, Work Breakdown Structure Element LBL-3.5 and under Contract No. DE-AC0376SF00098

ABSTRACT

The combined erosion-corrosion of a series of chromium bearing steels was investigated using a methane-air burner facility where cube shaped specimens were immersed in the combustion gas-solid particle flow. The specimens were mounted such that two front surfaces were impacted with the particles at an impingement angle of 45° and two back surfaces were protected from the particles, creating a static corrosion condition. Tests were performed using erodent particles from 5-100μm dia in size and test temperatures from 700° - 1000°C at a particle velocity of 5m/s.

It was determined that the corrosion mechanism dominated the surface degradation which occurred at all conditions tested for all alloys. The erosion process enhanced the growth of iron oxide crystallites on the scale surface and generally changed the morphology and chemical composition distribution of the scales. The larger erodent particles resulted in an increased scale thickness on the eroded-corroded surface compared to the scale thickness on the corroded only side.

INTRODUCTION

The erosion of ductile metals at both room and elevated temperatures has been studied and mechanisms for the erosion process developed.[1-5] Considerably less work has been done to determine how ductile metals behave under combined elevated temperature corrosion and erosion conditions.[6] This paper presents the results of tests performed under combined oxidation-erosion condition from 700° to 1000°C for 1018 steel and a number of chromium bearing steels having

from 2 1/4 to 18% chromium content. The morphology of the surface of the alloys under corrosion only and combined corrosion-erosion conditions on the same specimen in the same test is discussed.

No data on material loss rates were obtained during the series of tests reported. Also, no information is presented on the dynamic corrosion of the alloys where the corroding gas is impinged upon the specimen surface without eroding particles being present. The tests to determine loss rates and dynamic corrosion have not been completed yet. The morphologies of the surfaces of the various alloys tested are reported herein and constitute a valuable study in themselves.

TEST CONDITIONS

The test specimens of each alloy were exposed in the downstream duct of a methane-air burner operating with excess oxygen in the combustion gas. The exact partial pressure of oxygen was not determined. The specimens were 1.25cm on a side cubes with a small hole through their center for mounting on an alumina rod that extended into the 10cm dia. duct perpendicular to its wall. The specimens were exposed so that two of their sides were at 45° cycle to the exhaust gas and the other two sides were shielded from direct gas-particle impingement, thus providing two surfaces that were corroded-eroded and two surfaces that were only corroded. The ACES exhaust gas simulator at the Sandia Livermore National Laboratory Combustion Research Center was used for the tests. The specimens are shown during a test in Figure 1.

The conditions were:

- o gas - oxygen rich methane-air combustion gas
- o velocity of particles - 5m/s
- o particles - 5μm dia ave coal ash
  - 50, 100μm dia ave Al_2O_3
- o solids loading - 6g/min
- o test duration - 30 minutes
- o impingement angle - 45°
- o temperature differential across specimen - <6°C

After the test exposure the specimens were cooled in less than 1 minute after the gas-particle flow was turned off to temperatures <300°C where further corrosion could not occur, removed and the exposed surfaces microscopically analyzed using a scanning electron microscope (SEM).

RESULTS

The results of the tests will be presented as a function of the chromium content of the alloys tested, starting with 1018 plain carbon steel with a 0% Cr content. Table 1 lists the alloys tested and their compositions. Further, the results will be ordered by the test temperature, starting with the lowest temperature, 700°C. The patterns of behavior of the alloys appeared to follow these two variables in a somewhat orderly manner. The test temperatures, which ranged from 700°C for the 1018 to 1000°C for the 304SS are generally above the top service temperatures of the various alloys tested. They were selected to achieve oxidation rates which could be readily studied after the short 30 minute exposures in the burner duct. In all of the alloys

tested, corrosion was the dominant mechanism.

1018

Figure 2 shows the surfaces of the corroded and the eroded-corroded sides of a single specimen after exposure to the oxygen rich, methane-air combustion gases and 5μm ave dia coal ash particles at 700°C. The observed surface on both sides consisted of iron oxide, Fe_2O_3. The morphology of the scale on the corroded side consisted of a fine network of small needles with nodules of Fe_2O_3 penetrating up through them. A few coal ash particles from eddys in the flow behind the impingement sides of the specimen were also identified (the larger light nodules). The eroded-corroded side had the same fine needle network as the corroded side, but the larger Fe_2O_3 nodules were not present. A cross section of the scales to determine their thickness has not been made as yet. As can be seen corrosion was the dominant mechanism on both sides. The fine needles that occurred on the eroded side did not appear to be vulnerable to the impact force of the impinging coal ash particles.

2 1/4Cr1Mo

Figure 3 shows the surfaces of this alloy after the 700°C test. The appearance of the surface is essentially the same as was seen on the 1018 steel specimen. Figure 4 shows the same alloy after the 800°C test. The morphology of both surfaces has changed somewhat. On the corroded side the Fe_2O_3 needles have formed into an interlaced network with some individual needles of larger diameter also occurring. Very few nodules of Fe_2O_3 are observed along with a very few coal ash

particles (the larger, light grey particles in the lower photo).

On the eroded-corroded side, the morphology is somewhat different. The fine needle network appears to have condensed and a number of quite long comparatively large diameter, individual needles of oxide are seen growing out of the scale. Again, a few coal ash particles can be seen in the lower right photo. The delicacy of the long, individual needles on the eroded-corroded side is quite remarkable, considering that this side is being struck by coal ash particles. Note that the two lower photos are at the same magnification. The dynamic corrosion plus erosion that is occurring on the exposed side appears to be enhancing the growth of the oxide needles at this higher test temperature.

Figure 5 shows the SEM-KEVEX analysis of the surface scale on the eroded-corroded side of the specimen tested at 800°C. It can be seen that only iron oxide is present. The occurrence of only iron oxide on the surface with no chromium was observed for all of the alloys tested, except for the 304SS.

5Cr 1/2Mo

As the chromium content of the alloys increased the morphology of the oxide scale surface changed. The beginning of dramatic differences between the corroded side and the eroded-corroded side began with the 5Cr 1/2Mo steel. Figure 6 shows the corroded (above) and eroded-corroded (below) surface at two test temperatures, 800°C and 875°C.

At the 800°C test temperature, the needle-like network of the scale can be seen on both the corroded and eroded-corroded sides. A few nodules appear on the corroded side; none on the eroded-corroded side. The same thing occurred on the 1018 and 2 1/4Cr1Mo steels at the

lower, 700°C temperature (Figures 2 and 3). It appears that test temperature and chromium content trade off in the resultant oxide structures. As the chromium content increases, the surface morphology reverts back to that which occurred in the lower chromium content alloys at lower test temperatures.

At the 875°C test temperature, the next major change in the morphology occurred. The needles are almost non-existent on the corroded side (upper right photo) and they are replaced by nodules and columns of Fe_2O_3. The columns are different from the nodules in that their tops appear to be somewhat pointed and porous or wrinkled on the corroded side. The great difference in the morphology between the corroded and eroded-corroded sides first occurs on the eroded-corroded surface of this alloy. It consists entirely of crystalline columns of significantly greater cross section than the pointed-porous topped columns on the corroded side and their tops do not show any porosity. This intriguing behavior was observed on the higher chromium content alloys at higher test temperatures to an even greater degree, as will be seen.

9Cr1Mo

Figure 7 shows the extent to which the great difference occurred in the morphology between the corroded and eroded-corroded sides of the same test specimen. On the left side of the figure is the corroded side with a myriad of small diameter pointed-porous or wrinkled topped columns extending up perpendicular from the metal surface. The few gray globules are coal ash particles. On the right photo is the

eroded-corroded surface. The well defined crystalline columns of iron oxide (no chromium was determined) are many times the size of the columns on the corroded side and are no where near as numerous. Many of their tops have been chiselled away to form more or less points and no porosity or wrinkling can be observed at the tops of the columns. The action of the eroding coal ash particles can be seen to affect individual columns, but do not result in an overall eroding away of the surface. The relatively low density of the columns and their large size seems to reflect a selective thinning of the columns compared to the density of those that occurred on the corroded only side so that the remaining columns could grow to a much larger size. Whether this phenomenon, which is like the selective thinning of trees in a forest to promote the growth of the remaining ones, is the mechanism that is occurring is speculative at this time.

The determination of the composition of the columns on both the corroded and eroded-corroded sides of the 9Cr1Mo steel specimens was made by SEM-KEVEX analysis. Figure 8 shows the analyses of the scales that formed on the 9Cr1Mo steel. It can be seen that both types of columns are iron oxide with no chromium present. The presence of some coal ash is shown by the presence of such elements as Si, Ca, Al and Mg. The reason that the corroded side has more coal ash present is that the velocity of the particles on the back side of the specimens is much slower than on the front side that directly receive the impact of the coal ash at the full 5 m/s. The wafting particles on the back side can more readily get caught in the forest of columns that exists there.

The effect of test temperature on the morphology of the scales formed on the 9Cr1Mo steel are shown in Figure 9. On the left side are shown the surfaces after the 800°C test. Essentially the surface is a continuous Cr_2O_3 scale with some nodules of Fe_2O_3 and a few coal ash particles on the surface. The eroded-corroded side shows a slightly eroded Cr_2O_3 surface. At this lower temperature for the chromium content of the alloy, compared to the 925°C exposed specimen shown in Figure 8, the chromium is present in sufficient quantity to form a typical protective barrier type scale. The eroded-corroded side is still a mild enough overall condition to enable the alloy to maintain the protective scale.

When the test temperature is increased to 950°C (photos on the right side of Figure 9) the same type of behavior as was shown in Figure 7 is evident. In Figure 9 the magnification is higher than in Figure 7 and the nature of the columns can be more readily seen. Also, in the lower right photo another aspect of the erosion process is shown. In some isolated areas the columns had been eroded away, leaving a more continuous scale showing beneath them. The contours appearing on the scale layer is direct evidence of the erosion process. The overall differences between the surface morphologies of both the corroded and eroded-corroded specimens at the two test temperatures is most intriguing.

410SS

The 410SS specimens showed the same type of behavior as the lower chromium content, ferritic steels that formed columns. Figure 10 shows the two surfaces after testing at 950°C. The chiselled tops of the eroded-corroded side columns toward pointed shapes are clearly evident as are their greatly increased size over the corroded side columns. Note the difference in magnification at both the lower and the higher magnifications. At least one of the columns (lower right side photo) is cracked, providing a short circuit diffusion path.

The ability of the large diameter, dense columns that form on the eroded-corroded side to possibly retard metal surface retardation from erosion once they form is an interesting speculation. On the other hand, the increased diffusion rates in the dense columns to enhance corrosion is a distinct possibility, as will be discussed later. The basis for the retardation of the erosion process is contained in Ref. 7 where it was reported that dense, columnar NiO scale on a nickel substrate eroded at substantially lower rates than equiaxed, porous NiO.

Even with a 12% Cr content in the alloy, the columns of oxide were determined to be pure iron oxide. Figure 11 shows the SEM-KEVEX peak analyses. It is interesting to note, however that the No. 2 peak on the eroded corroded side shows some chromium in a crystallite that appears to be below the general level of the columns. Again, some coal ash was retained on the corroded side of the specimen, peak 2 where the velocities are very low.

The 410SS specimens were cross sectioned to determine the nature

of the scale down to the base metal. Cross sectional analyses of the other exposed alloys is in process. Figure 12 shows the morphology of the scales and the distribution of iron and chromium through them. Analysis of the photos indicates that combined erosion-corrosion not only changes the surface morphology of the scale compared to straight corrosion, but also the cross section morphology and composition.

On the corroded side (left photos) the secondary electron image indicates that there is a duplex scale present with a line of porosity separating the two phases. Analyzing the x-ray maps shows that the top layer is iron oxide with no chromium in it, as has been discussed above. However, the second layer of the scale has substantial chromium content and is probably an iron-chromium oxide spinel. This layer has a scalloped, intimate bonded interface with the base metal. The cross sections of the small, pointed columns of surface scales described earlier can be readily seen in the upper left photo.

The morphology of the scale cross section on the eroded-corroded side of the specimen is quite different from that on the corroded only surface. On the right hand side of Figure 12 is the secondary electron image and iron and chromium x-ray maps of the eroded-corroded scale. The cross sections of the much larger columns can be seen at the top of scale cross section, verifying the observations made earlier concerning the morphology differences between the surface of the corroded and eroded-corroded scales.

Referring to the x-ray maps, it can be seen that the total scale thicknesses of the corroded and eroded-corroded sides as well as the distribution of the two phases on each side

are markedly different. The iron oxide scale is much thinner on the erosion-corrosion side, extending only to the base of the columns. This accounts for the occurrence of the chromium peak in the surface side analysis shown in Figure 11. The Fe-Cr spinel layer is much thicker on the eroded-corroded side, essentially constituting the main body of the scale. Also, the interface between the lower layer of the duplex scale and the base metal is quite porous on the erosion-corrosion side. Thus the occurrence of erosion in conjunction with corrosion, with the corrosion process dominant, changes the morphology and the composition distribution of the scale that is formed.

304SS

The 304SS, an austenitic alloy with a significantly higher chromium content than any of the chromium containing ferritic alloys tested, behaved in a somewhat different manner than the other steels at temperatures higher than were used to test the other steels. Figure 13 shows that the surfaces developed a continuous Cr_2O_3 scale on both the corroded and eroded-corroded surfaces and that the barrier scale was not penetrated by the eroding particles.

On both the corroded and eroded-corroded surfaces, nodules of iron-chromium spinel have penetrated through the Cr_2O_3 scale layer. The size of the nodules is considerably larger on the erosion-corrosion surface than on the corroded surface. This follows the general trend throughout the test series of having combined erosion-corrosion enhance the growth of individual crystallites on the scale outer surface. Some of the nodules present on the surface are coal ash.

Laser Raman spectroscopy was used to identify the phases that were present on the surface of the 304SS test samples. Figure 14 shows the Raman spectra for the corroded surface. The peak at 570 is Cr_2O_3, the peak at 660 is spinel and the small peak at 1010 represents the compounds in coal ash. Figure 15 shows the Raman spectra of an area on the surface of the eroded-corroded side. The additional peaks over and above those that occurred in Figure 14 are due to coal ash particles adhering to the surface. These spectra indicate that iron-chromium spinel individual nodules formed on the iron-chromium-nickel 304SS rather than the iron oxide nodules that formed on the straight iron-chromium alloys.

PARTICLE SIZE EFFECT

In order to determine what type of scale morphology would occur on the eroded-corroded surfaces when larger eroding particles were used which could transfer a greater force to the surface upon impact, 50μm and 100μm Al_2O_3 particles were used to erode 410SS. All of the other test conditions were the same as were used in the 5μm coal ash tests. It was thought that while the small, 5μm coal ash particles used in the earlier tests were too small to result in erosion being the dominant mechanism, the larger particles could change that circumstance.

Figure 16 shows the eroded-corroded surface of the 410SS after exposure to the three different size particles. It can be seen that as the particle size and its resultant impact force increased, the individual columns of iron oxide became smaller, almost disappearing in

the 100μm Al_2O_3 erodent particles test. The greater impact force of the 100μm Al_2O_3 particles also cracked the scale that had formed, providing excellent short circuit diffusion paths for corrosion.

Figure 17 shows the cross section of the scales formed on the corroded and eroded-corroded surfaces of the 410SS. The corroded surface scale is similar to the scale shown in Figure 12. The small diameter columns that can be seen in Figure 12 were probably knocked off by 100μm Al_2O_3 particles that lightly struck the back surface of the specimen as the result of eddying of the gas-particle stream. The light impacts could also have caused the relatively large size voids seen in Figure 12 to crack through and result in the separation of scale layers seen in Figure 17.

The cross section of the eroded-corroded side of the 410SS specimen in Figure 17 has three significant differences from the eroded-corroded surface shown in Figure 12. First, the scale is considerably thicker on the eroded-corroded side than it is on the just corroded side. Note the difference in magnification of the micrographs in Figure 17. The scale on both sides of the specimen were much nearer in thickness for the 5μm coal ash erosion tests. It appears that the more severe erosion conditions that occurred when the 100μm size particles were used enhanced the corrosion rate, maybe as the result of cracking the coating as was shown in Figure 16 which increased the short circuit diffusion which could occur. Definitive metal surface regression rates tests will have to be performed to establish better exactly what is happening.

Second, the iron oxide scale layer is quite thick on the erosion-

corrosion surface compared to the spinel layer in Figure 17. This was not the case for the 5μm coal ash tests, as shown in Figure 12, where the iron oxide scale layer became quite thin on the eroded-corroded surface compared to the spinel layer. Third, the major porosity at the scale-metal interface which was observed in Figure 12 did not occur in the 100μm Al_2O_3 erodent tests as can be seen in Figure 17. Instead, it appears that areas of very small pores formed in the spinel layer near the scale metal interface.

DISCUSSION

The observations that have been reported in this paper on the nature of the combined erosion-corrosion process in chromium bearing steels have not been seen before. Therefore, the interpretations of causes and effects are speculative at this time. Much work remains to be done before absolute mechanisms can be defined and the effect of the observed behavior on materials performance in industrial applications known. Still, a significant start has been made to understand the effects of combined erosion-corrosion on materials. Some of the observations of the combined behavior that are of particular interest are discussed in this section. The dominance of the corrosion process at all conditions of temperature, alloy composition, particle size and other erosion conditions was unexpected. It was thought that when at least the 100μm Al_2O_3 particles were used, the erosion process would be able to sweep oxide off the surface as it formed. The mechanism of elevated temperature corrosion when the oxidizing surface is being mechanically affected during the process must follow different rate laws than those that have been determined to be applicable to

static corrosion. Parabolic and linear rates of corrosion are probably replaced by accelerating rates of some type which are not defineable at this time.

One of the problems that is associated with determining the kinetics of the corrosion process is the inability to precisely measure the metal surface regression rate. The best kinetic work in straight corrosion is carried out using weight change measurements. In a combined erosion-corrosion test, the specimen is undergoing different reactions on its various surfaces and weight change measurements are not appropriate. Efforts are underway to develop an alternative method to measure the rates in a precise enough manner to use for kinetic analysis.

A pattern developed in the test series using 5μm coal ash particles that somewhat related the scale morphology to the test temperature, chromium content of the alloy and whether static corrosion or combined erosion-corrosion was occurring. Its meaning, if indeed there is one, is not known. As the chromium content, the test temperature and the severity of the surface environment (corrosion compared to erosion-corrosion) increased, the dominant shape of the iron oxide particles on the surface progressed from nodules to needles to columns. A less than thorough review of the literature failed to shed light on why this pattern occurred.

The change in the composition as well as the morphology of the surface scale as the result of the combined erosion-corrosion process (Figure 12) is a very interesting phenomenon that requires more work before it is understood. The effects of the gross changes which

occurred in the scales on the surface regression rate of the metal surface should be determined. Even though the scale thickness on the erosion-corrosion surface is considerably greater than it is on the corroded surface, the overall metal regression rate could be retarded by the formation of the large, dense crystals of iron oxide on the surface (Reference 7).

CONCLUSIONS

1. Corrosion is the dominant mechanism of surface degradation in combined erosion-corrosion tests over the range of test conditions used in this investigation.

2. Erosion using 100μm dia particles in combination with corrosion results in thicker oxide scales forming than were observed to form on statically corroded surfaces.

3. A great increase in the size of the iron oxide crystallites as well as a change in their shape occurred on the oxide scale surface as the result of erosion occurring along with corrosion when 5μm coal ash particles were used.

4. As the eroding particles increased in size to 100μm dia, the eroded-corroded surface of the scale became considerably less textured than occurred when 5μm dia particles were used.

5. As the test temperature and the chromium content of the alloys increased, the dominant shape of the iron oxide particles on the surface of the scale progressed from nodules to needles to columns. The reason for this and its meaning are not know.

6. Considerably more work has to be done before the phenomina which were observed in this test series are well understood.

REFERENCES

1. Levy, A., paper presented at NACE Conference, Berkeley, California, Jan. 1982, p. 298.

2. Ives, L., paper presented at the ASME Annual Meeting, Dec. 1976.

3. Foley, T., Levy, A. Wear Vol 91, No. 1, p 45.

4. Quadir, T., Shewmon, P. Met. Trans. A., Vol 12A, p 1176, (1981).

5. Brown, R. Edington, J. Wear Vol 77, No. 3, p. 1163 (1982).

6. Wright, I. Herchenroeder, R. High Temperature Erosion-Corrosion of Alloys, EPRI Report CS-1454, July 1980.

7. Zambelli, G., Levy A. Wear Vol 68, No. 3, p 305 (1981).

ACKNOWLEDGMENT

Research sponsored by the U.S. Department of Energy under DOE/FEAA 15 10 10 0, Advanced Research and Technical Development, Fossil Energy Materials Program, Work Breakdown Structure Element LBL-3.5 and under Contract No. DE-AC03-76SF00098.

FIGURES

TABLE 1

ALLOY COMPOSITION (NOMINAL)

ALLOY	Cr	Ni	Mo	Si	Mn	C	P/S max	Fe
1018					0.5	0.2	0.09	bal
2 1/4Cr 1Mo	2.2		0.9	0.3	0.4	0.2	0.02	bal
5Cr 1/2Mo	5.1		0.6	0.02	0.5	0.1	0.02	bal
9Cr 1Mo	9		1.0	0.5	0.5	0.15	0.02	bal
410SS	12			1.0	1.0	0.2	0.1	bal
304SS	18	9		1.0	2.0	0.1	0.1	bal

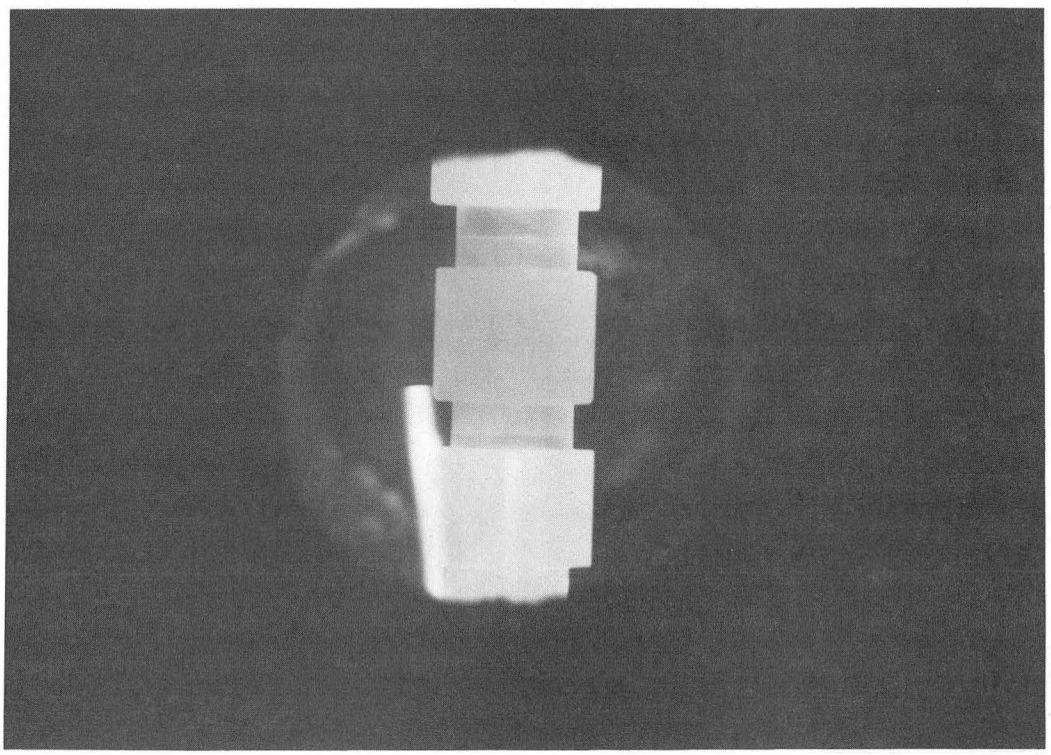

CBB 834-3754

Fig. 1. Specimens in burner duct during testing

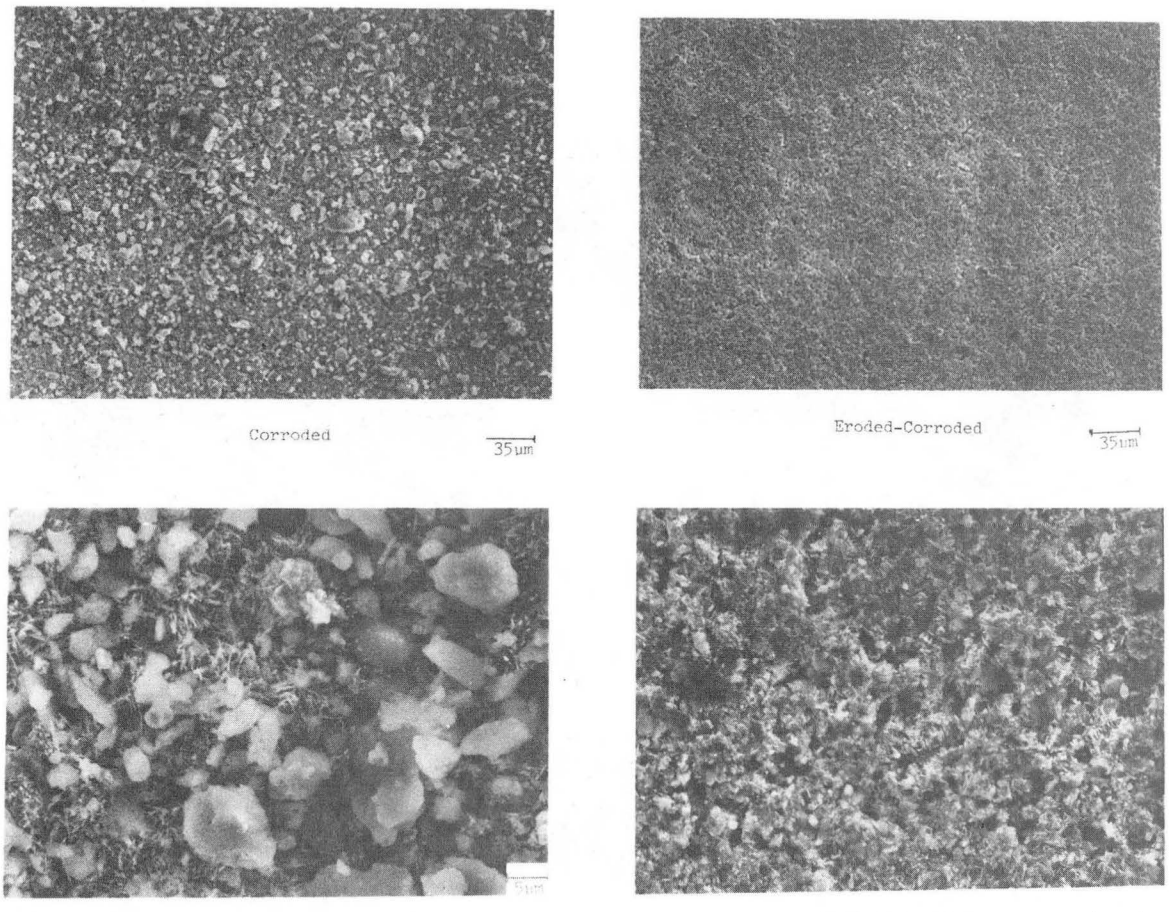

Fig. 2. Corroded and eroded-corroded surfaces of 1018 steel at 700°C

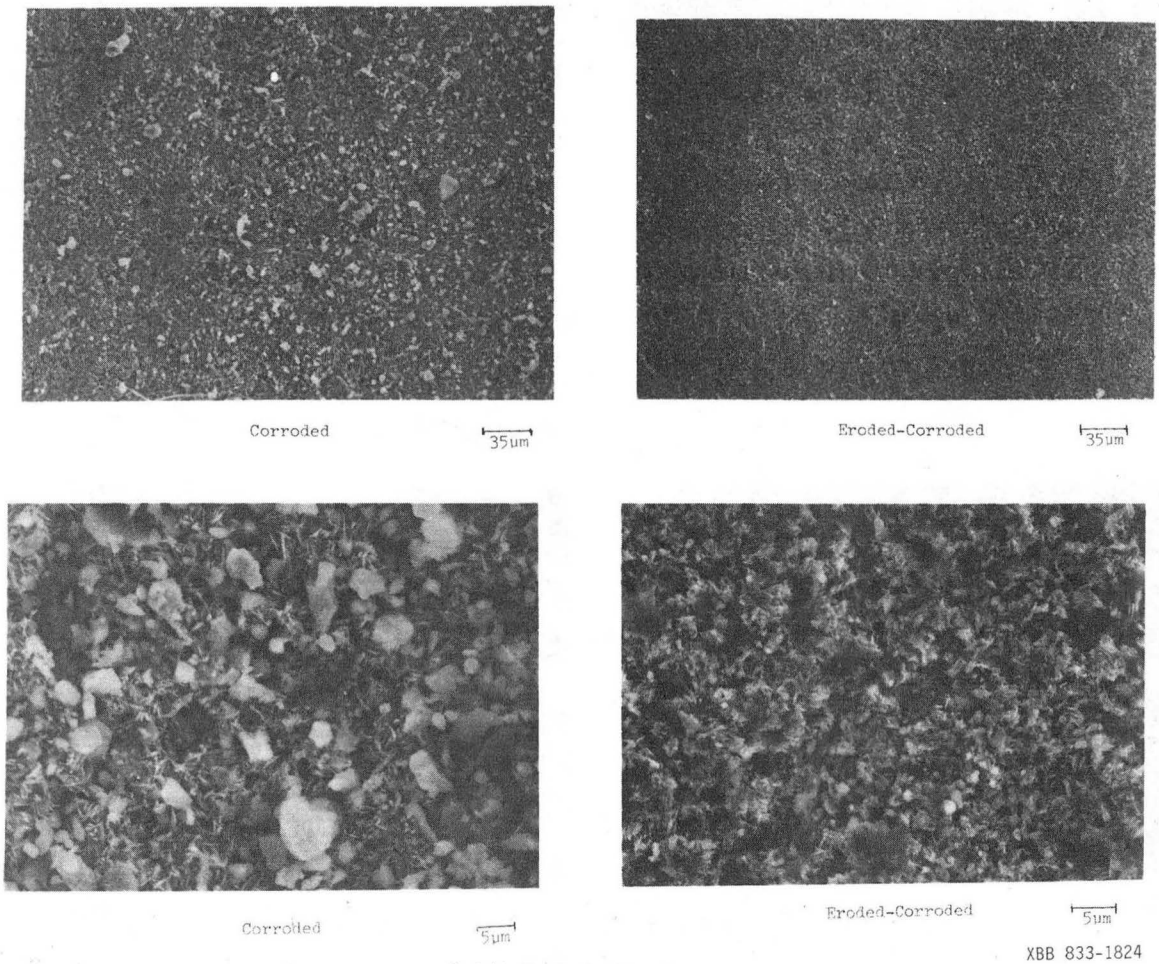

Fig. 3. Corroded and eroded-corroded surfaces of 2 1/4 Cr 1Mo steel at 700°C

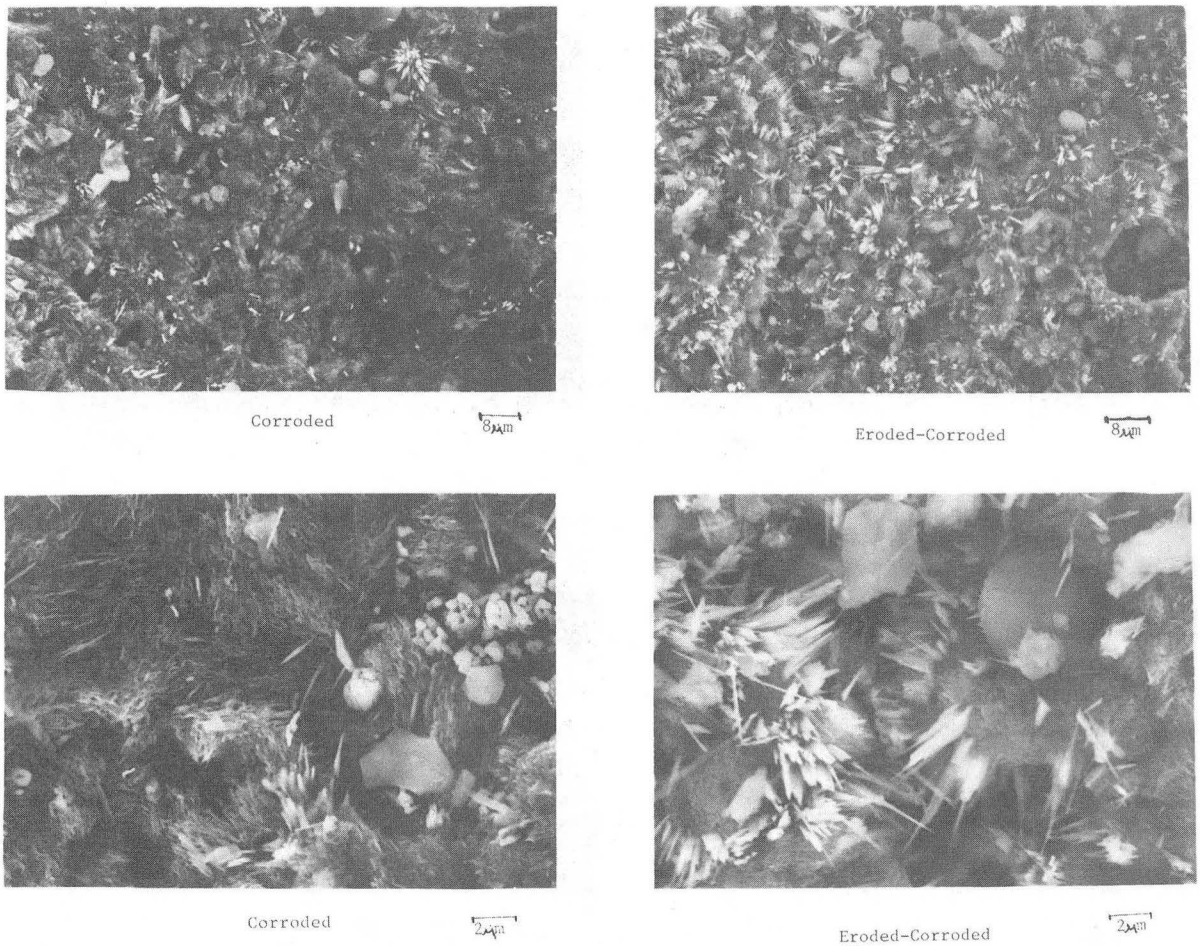

Fig. 4. Corroded and eroded-corroded surfaces of 2 1/4 Cr 1Mo steel at 800°C

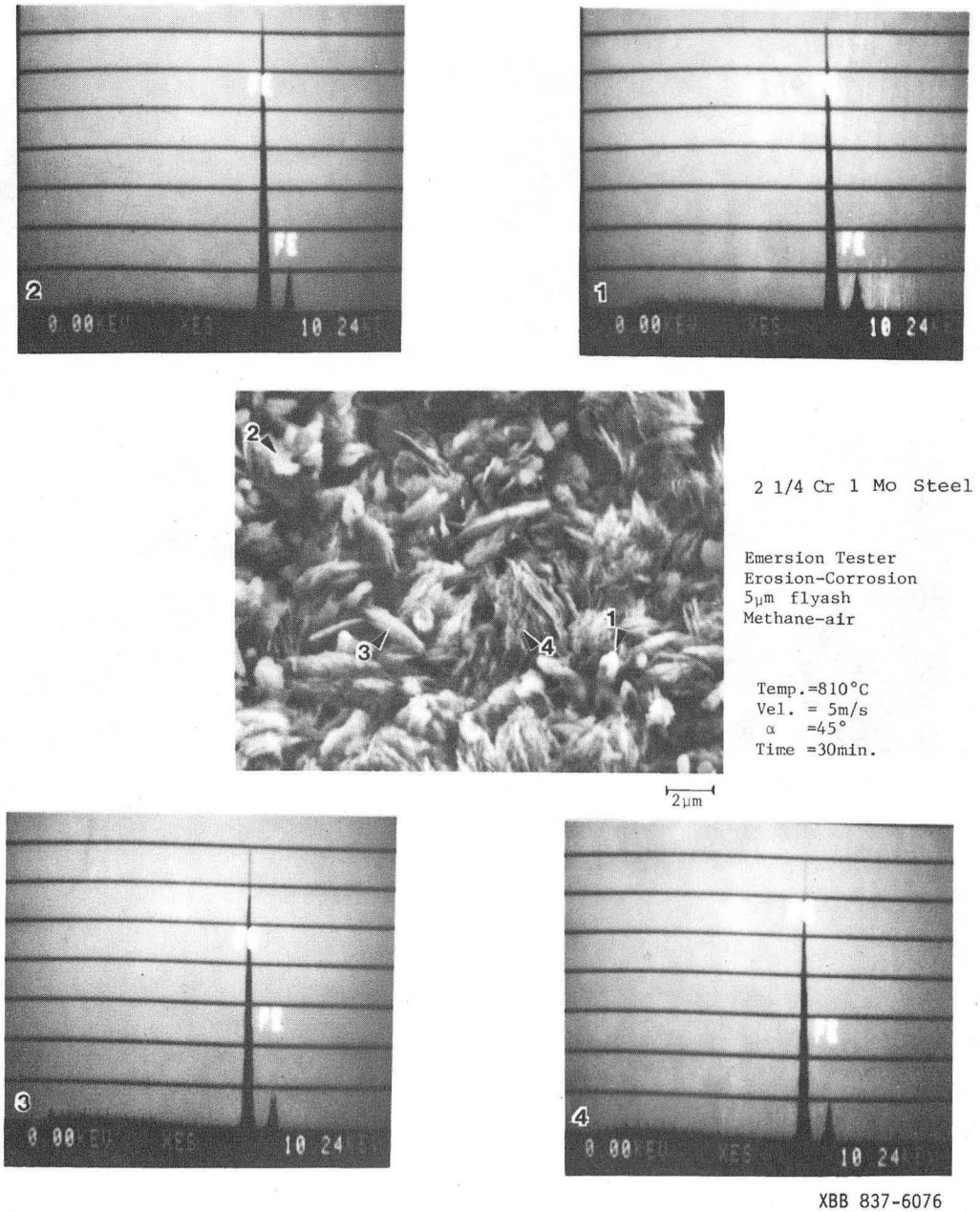

Fig. 5. SEM-KEVEX analysis of scale surface on eroded-corroded side of the 2 1/4 Cr 1Mo steel at 800°C

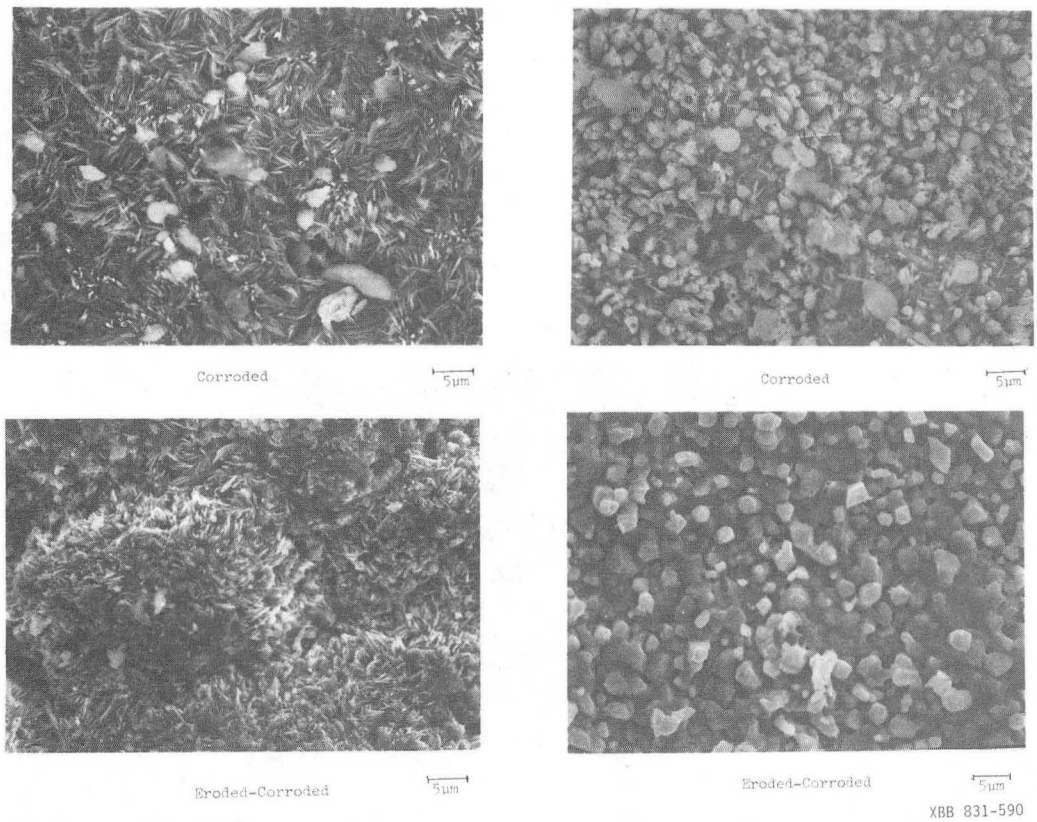

Fig. 6. Corroded and eroded-corroded surfaces of 5 Cr 1/2Mo steel at 800°C and 875°C

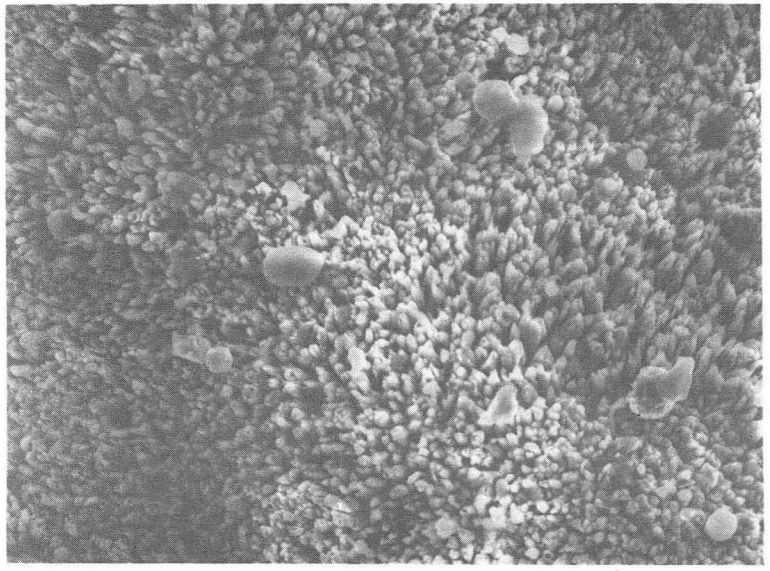

Corroded

10μm

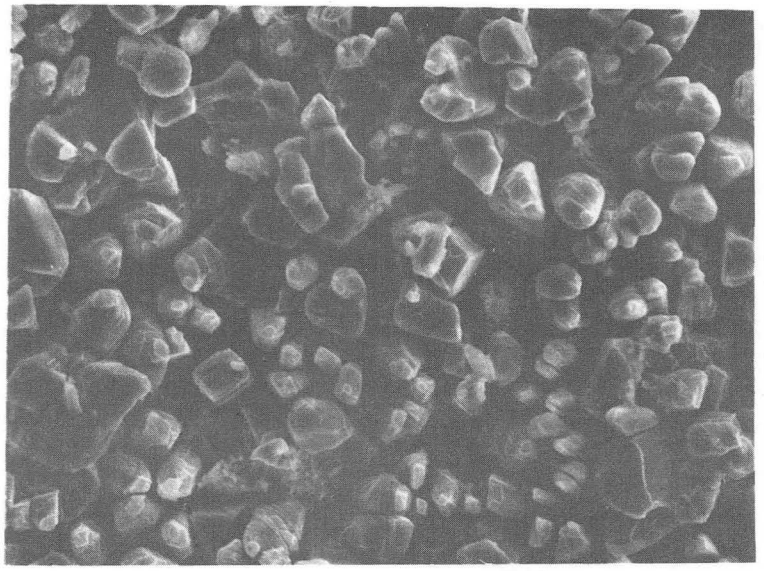

Eroded-Corroded

10μm

9 Cr 1 Mo Steel

Emersion Tester	Temp. =925°C
5μm flyash	Vel. = 5m/s
Methane-air	α =45°
	Time =30min.

Fig. 7. Corroded and eroded-corroded surfaces of 9 Cr 1Mo steel at 925°C XBB 820-9329

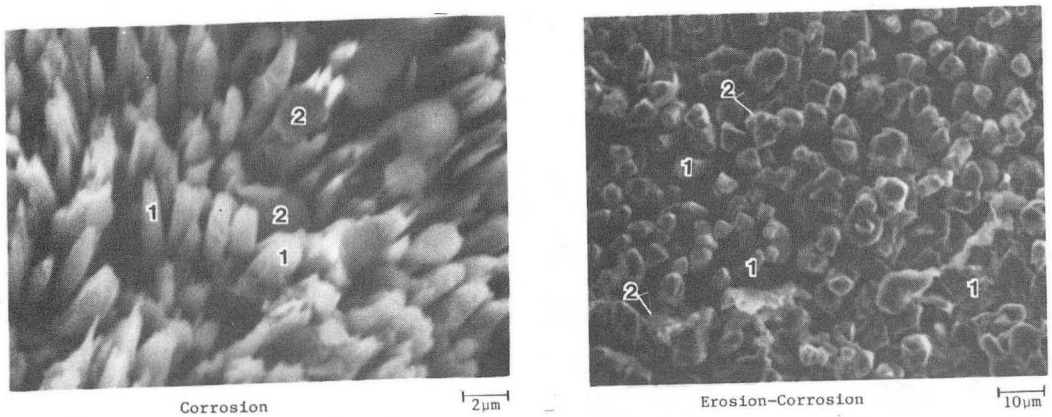

XBB 837-6078

Fig. 8. SEM-KEVEX analyses of the oxide column composition of the 9 Cr 1Mo steel at 950°C

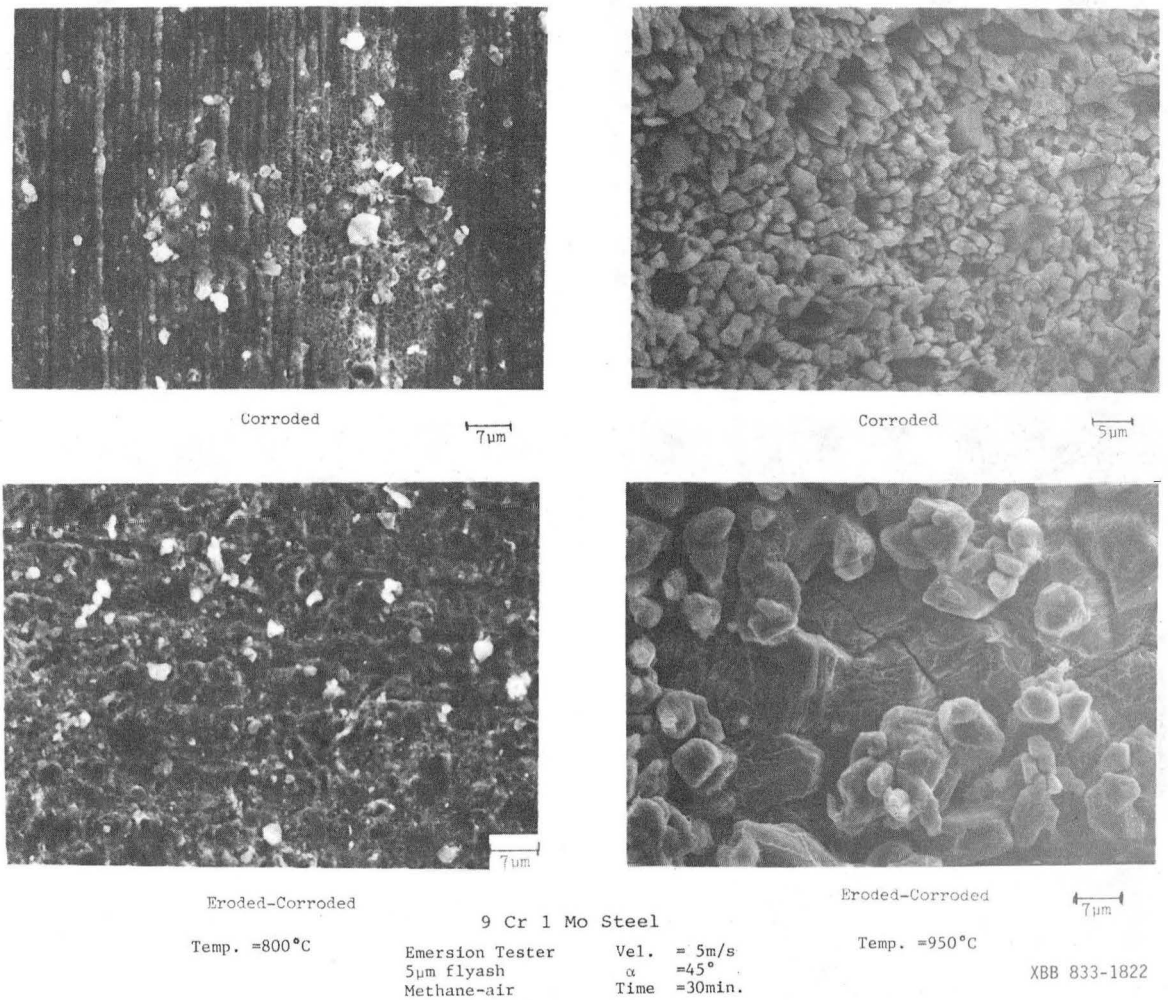

Fig. 9. Corroded and eroded-corroded surfaces of 9 Cr 1Mo steel at 800°C and 950°C

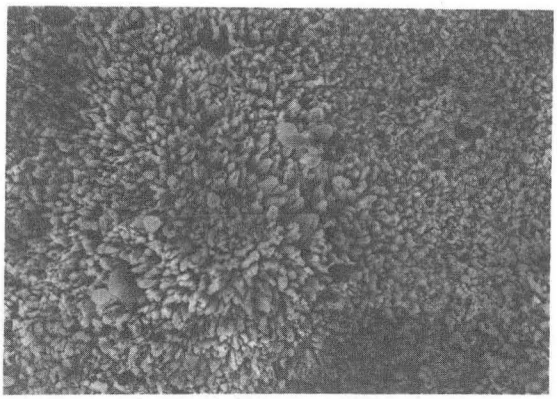

Corroded 10μm

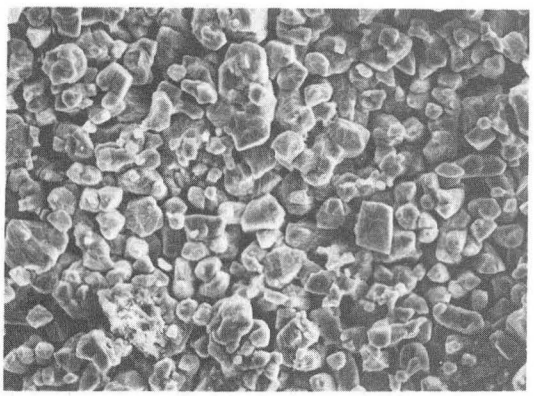

Eroded-Corroded 20μm

Corroded 3μm

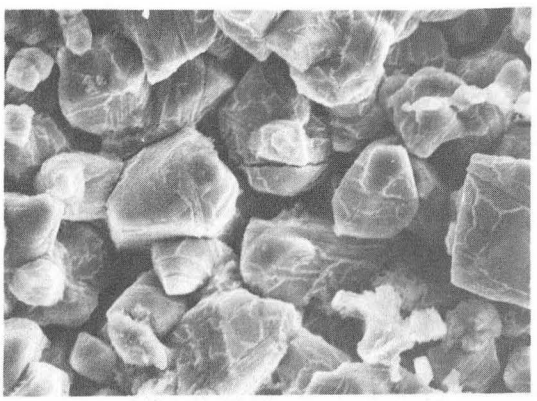

Eroded-Corroded 8μm

410 SS

Emersion Tester	Temp. =950°C
5μm flyash	Vel. = 5m/s
Methane-air	α =45°
	Time =30min

Fig. 10. Corroded and eroded-corroded surfaces of 410SS at 950°C XBB 820-9325

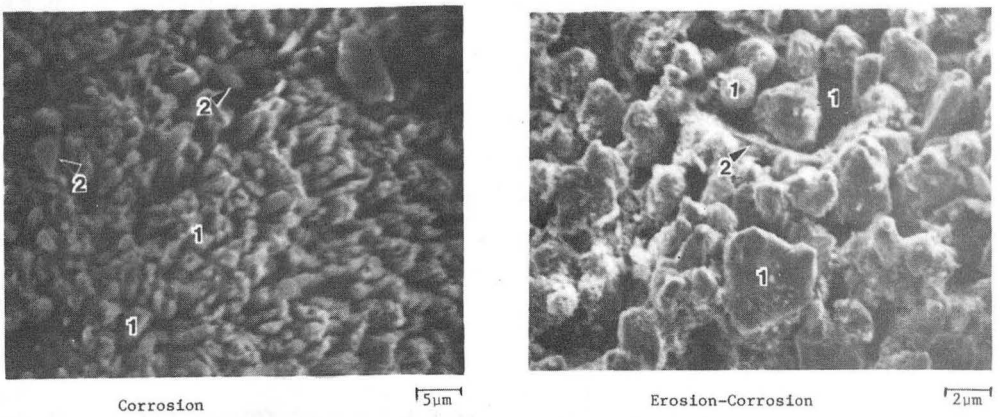

Fig. 11. SEM-KEVEX analyses of columns of scale on 410SS at 950°C

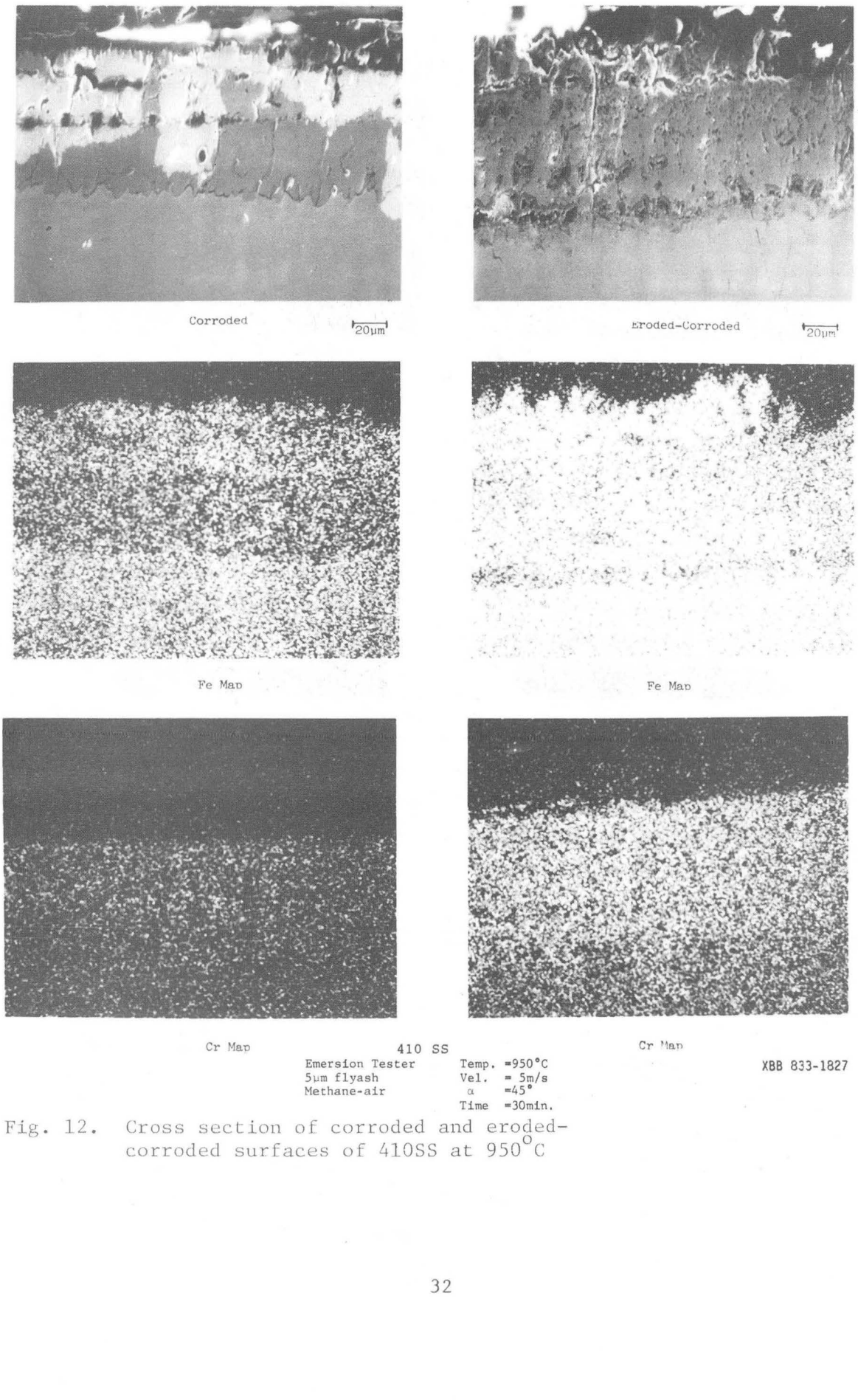

Fig. 12. Cross section of corroded and eroded-corroded surfaces of 410SS at 950°C

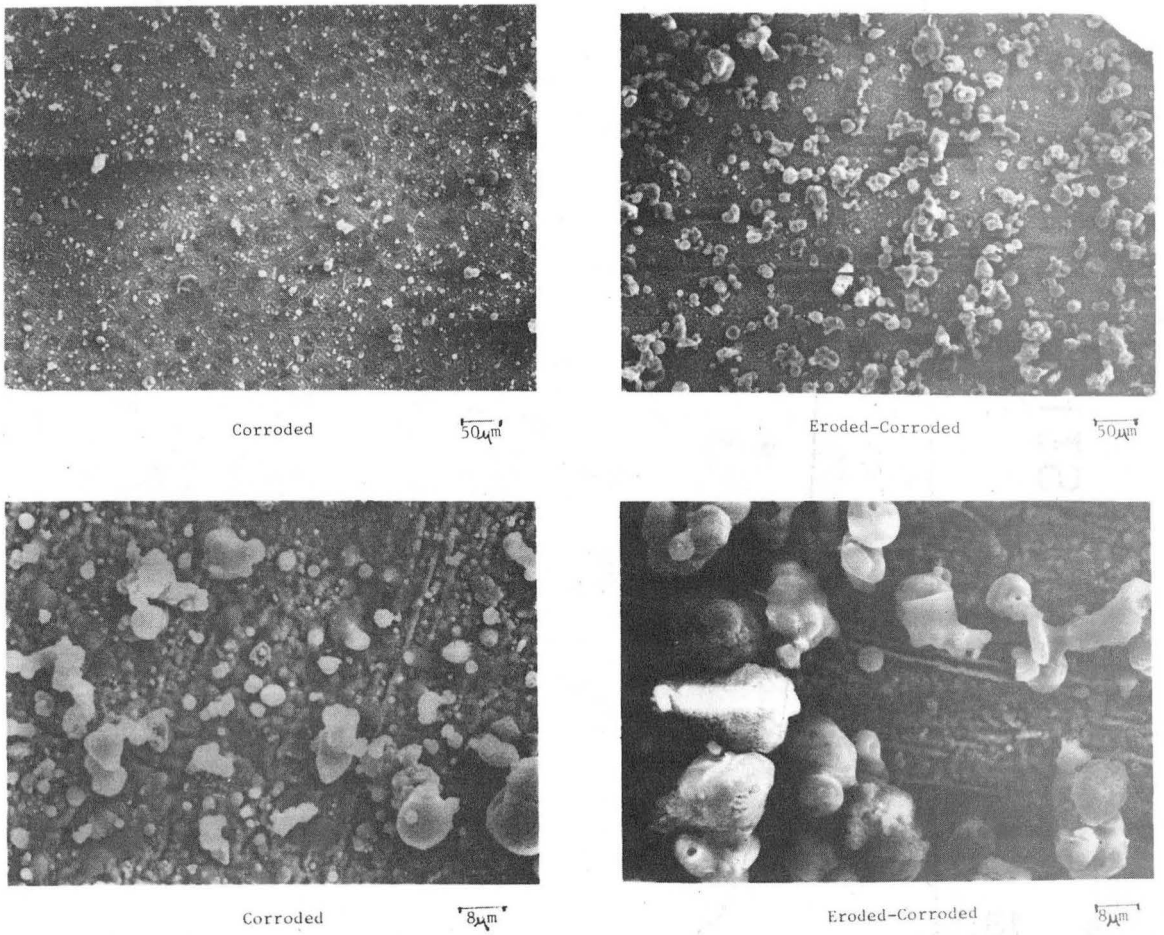

Fig. 13. Corroded and eroded-corroded surfaces of 304SS at 1000°C

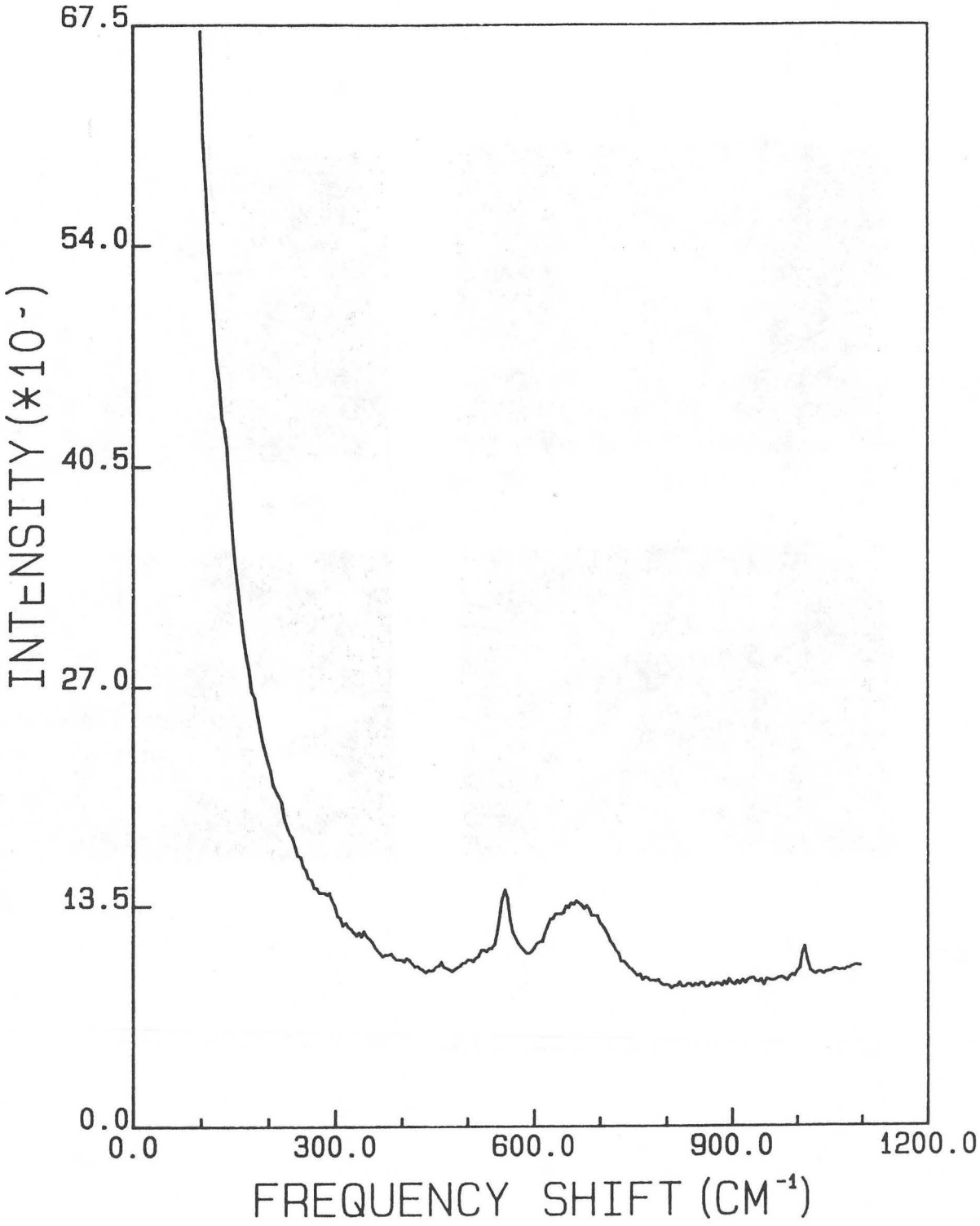

XBL 837-10812

Fig. 14. Raman spectra of corroded surface of 304SS at 1000°C

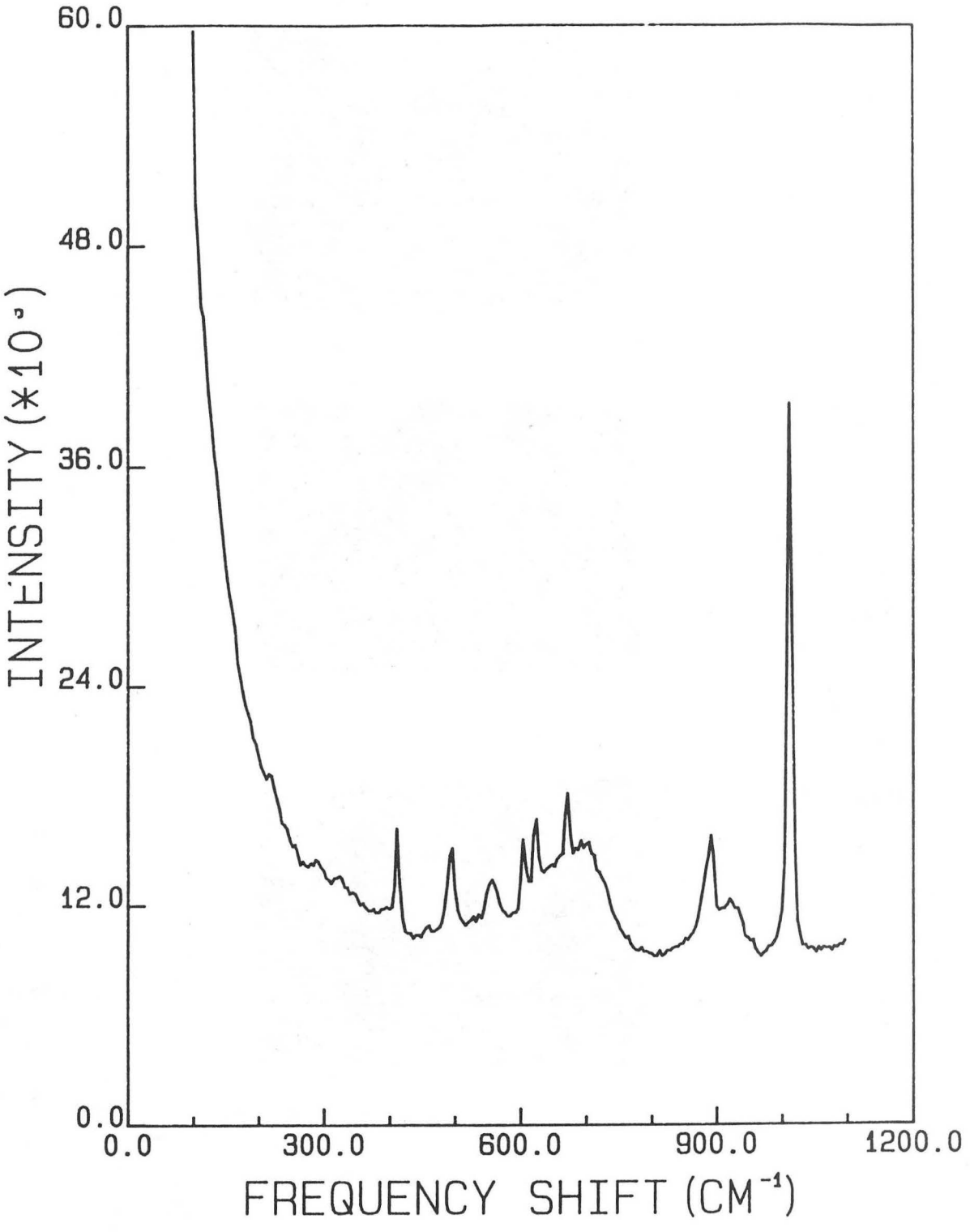

XBL 837-10813

Fig. 15. Raman spectra of eroded-corroded surface of 304SS at 1000°C

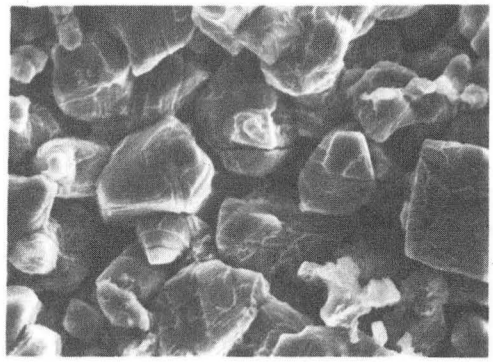

5μm flyash

5μm

50μm Al_2O_3

3μm

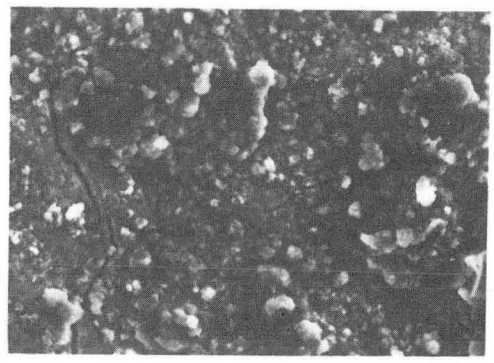

100μm Al_2O_3

15μm

410 SS

Emersion Tester	Temp.	=950°C
Erosion-Corrosion	Vel.	= 5m/s
Methane air	α	=45°
	Time	=30min.

XBB 837-6248

Fig. 16. Effect of eroding particle size on the surface morphology of the eroded-corroded surface of 410SS at 950°C

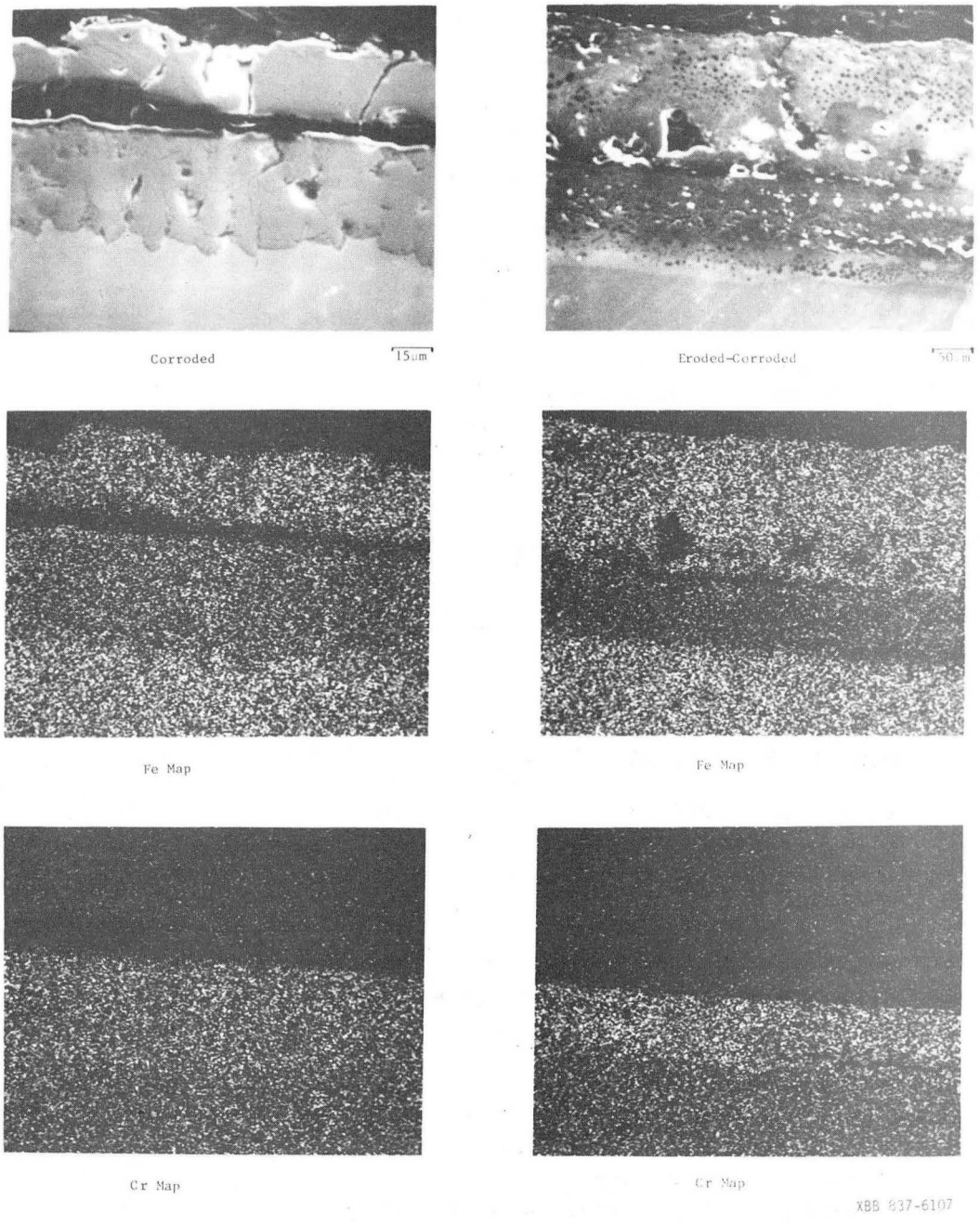

Fig. 17. Cross sections of corroded and eroded-corroded scale on 410SS at 950°C eroded by 100 μm Al_2O_3 particles

DISTRIBUTION LIST

Wate Bakker
EPRI
3214 Hillview Avenue
P.O. Box 10412
Palo Alto, CA 94304

B.R. Banerjee
Ingersoll-Rand Company
P.O. Box 301
Princeton, NJ 08540

K.L. Baumert
Air Products & Chemicals, Inc.
P.O. Box 538
Allentown, PA 18105

S.M. Benford
NASA Lewis Research Center
21000 Brookpark Road
Cleveland, OH 41135

A.E. Biggs
Arco Chemicals
3801 W. Chester Pike
Newtown Square, PA 19073

R. Blickensderfer
Bureau of Mines
P.O. Box 70
Albany, OR 97321

R.A. Bradley, Manager
Fossil Energy Materials Program
Oak Ridge National Laboratory
P.O. Box X
Oak Ridge, TN 37830

Richard Brown
Materials Laboratory
Department of Chemical Engineering
University of Rhode Island
Kingston, RI 02881

DISTRIBUTION LIST cont'd

D.H. Buckley
NASA Lewis Research Center
21000 Brookpark Road
Cleveland, OH 41135

P.T. Carlson, Task Leader
Fossil Energy Materials Program
Oak Ridge National Laboratory
P.O. Box X
Oak Ridge, TN 37830

J. Carpenter
ECUT Program
Oak Ridge National Laboratory
P.O. Box X
Oak Ridge, TN 37830

J.P. Carr
Department of Energy, Office of Fossil Energy
FE-42 Mailstop 3222-GTN
Washington, DC 40525

Hans Conrad
Materials Engineering Department
North Carolina State University
Raleigh, NC 27659

P. Crook
Cabot Corporation
Technology Department
1020 W. Park Avenue
Kokomo, IN 46901

S.J. Dapkunas
Department of Energy, Office of Fossil Energy
Technical Coordination Staff FE-14
Mailstop C-156 GTN
Washington, DC 40525

DOE Technical Information Center
P.O. Box 62
Oak Ridge, TN 37830

W.A. Ellingson
Argonne National Laboratory
9700 South Cass Avenue
Argonne, IL 60439

DISTRIBUTION LIST cont'd

J. Gonzales
GTE
Chemical & Metallurgical Division
Hawes Street
Towanda, PA 18848

Å. Hammarsten
Teknikum
P.O. Box 534, S-751 21
Uppsala
SWEDEN

E. Haycock
Westhollow Research Center
Shell Development Company
P.O. Box 1380
Houston, TX 77001

J.M. Hobday
Department of Energy
Morgantown Energy Technology Center
P.O. Box 880
Morgantown, WV 26505

E.E. Hoffman, Manager
National Materials Program
Department of Energy
Oak Ridge Operations
P.O. Box E
Oak Ridge, TN 37830

J.A.C. Humphrey
Mechanical Engineering Department
University of California
Berkeley, CA 94720

I.M. Hutchings
University of Cambridge
Department of Metallurgy
Pembroke Street
Cambridge
ENGLAND

Sven Jansson
Stal-Laval Turbin AB
Finspong S-61220
SWEDEN

DISTRIBUTION LIST cont'd

R.R. Judkins
Fossil Energy Materials Program
Oak Ridge National Laboratory
P.O. Box X
Oak Ridge, TN 37830

M.K. Keshavan
Union Carbide Corporation
Coating Services Department
1500 Polco Street
Indianapolis, IN 46224

T. Kosel
University of Notre Dame
Dept. of Metallurgical Engineering
& Materials Science
Box E
Notre Dame, IN 46556

L. Lanier
FMC-Central Engineering Laboratory
1185 Coleman Avenue
Santa Clara, CA 95052

N.H. MacMillan
Pennsylvania State University
167 Materials Research Laboratory
University Park, PA 16802

P.K. Mehrotra
Kennemetal Inc.
1011 Old Salem Road
Greensburg, PA 15601

Ken Magee
Bingham-Williamette Co.
2800 N.W. Front Avenue
Portland, OR 97219

T. Mitchell
Case Western Reserve University
Department of Metallurgy
Cleveland, OH 44106

Fred Pettit
Dept. of Metallurgy & Materials Engineering
University of Pittsburgh
Pittsburgh, PA 15261

DISTRIBUTION LIST cont'd

R.A. Rapp
Metallurgical Engineering
116 W. 19th Avenue
The Ohio State University
Columbus, OH 43210

D.A. Rigney
Metallurgical Engineering
116 W. 19th Avenue
The Ohio State University
Columbus,OH 43210

A.W. Ruff
Metallurgy Division
National Bureau of Standards
B-266 Materials
Washington, DC 20234

Alberto Sagüés
IMMR - University of Kentucky
763 Anderson Hall
Lexington, KY 40506

Gordon Sargent
University of Notre Dame
Dept. of Metallurgical Engineering & Materials Science
Box E
Notre Dame, IN 46556

Paul Shewmon
Dept. of Metallurgical Engineering
116 W. 19th Avenue
Columbus, OH 43210

Gerry Sorell
EXXON Research & Engineering Company
P.O. Box 101
Florham Park, NJ 07932

John Stringer
University of California
Lawrence Berkeley Laboratory
Mailstop 62/203
Berkeley, CA 94720

Widen Tabakoff
Dept. of Aerospace Engineering
University of Cincinnati
Cincinnati, OH 45221

DISTRIBUTION LIST cont'd

Edward Vesely
IITRI
10 West 35th Street
Chicato, IL 60616

J.J. Wert
Metallurgy Department
Vanderbilt University
P.O. Box 1621, Sta. B
Nashville, TN 37235

J.C. Williams
Dept. of Metallurgy & Materials Science
Carnegie-Mellon University
Schenley Park
Pittsburgh, PA 15213

S. Wolf
Department of Energy
Basic Energy Sciences Office
Division of Materials Sciences
Washington, DC 20545

Ian Wright
Materials Science Division
Battelle Memorial Institute
505 King Avenue
Columbus, OH 43201

C.S. Yust
Metals and Ceramics Division
Oak Ridge National Laboratory
P.O. Box X
Oak Ridge, TN 37830

This report was done with support from the Department of Energy. Any conclusions or opinions expressed in this report represent solely those of the author(s) and not necessarily those of The Regents of the University of California, the Lawrence Berkeley Laboratory or the Department of Energy.

Reference to a company or product name does not imply approval or recommendation of the product by the University of California or the U.S. Department of Energy to the exclusion of others that may be suitable.

TECHNICAL INFORMATION DEPARTMENT
LAWRENCE BERKELEY LABORATORY
UNIVERSITY OF CALIFORNIA
BERKELEY, CALIFORNIA 94720